RESEARCH ARTICLE | FEBRUARY 03 2025

An oscillation flow mechanism of hypersonic flows over parallel-staged double-wedge configuration ⊘

Yue Wang (王粤) ⓘ ; Yiming Liu (刘一鸣) ⓘ ; Haojie Li (李豪杰) ⓘ ; Xiaopeng Xue (薛晓鹏) ✉ ⓘ ;
Yunpeng Wang (汪运鹏) ⓘ

Check for updates

View Online

Export Citation

Articles You May Be Interested In

KoopmanLab: Machine learning for solving complex physics equations

APL Mach. Learn. (September 2023)

Experimental realization of a quantum classification: Bell state measurement via machine learning

APL Mach. Learn. (September 2023)

AIP Publishing

Physics of Fluids

Special Topics Open for Submissions

Learn More

AIP Publishing

An oscillation flow mechanism of hypersonic flows over parallel-staged double-wedge configuration

Yue Wang (王粤),[1,2] (iD) Yiming Liu (刘一鸣),[1,2] (iD) Haojie Li (李豪杰),[1,2] (iD) Xiaopeng Xue (薛晓鹏),[3,a] (iD) and Yunpeng Wang (汪运鹏)[1,2] (iD)

AFFILIATIONS

[1]State Key Laboratory of High Temperature Gas Dynamics, Institute of Mechanics, Chinese Academy of Sciences, Beijing 100190, China
[2]School of Engineering Science, University of Chinese Academy of Sciences, Beijing 100049, China
[3]School of Automation, Central South University, Changsha 410083, China

[a]Author to whom correspondence should be addressed: xuexiaopeng@csu.edu.cn

ABSTRACT

A two-body model is an essential configuration of the aerospace vehicle, e.g., two-stage-to-orbit vehicle. Unsteady numerical simulations are performed to investigate the hypersonic flow over a parallel-staged double-wedge configuration of the different angles of incidence (AoI) at Mach 7. The effect of the AoI on the unsteady flow is analyzed, and the flow mechanism of the periodic flow oscillation associated with shock interactions is clarified. The unsteady oscillation flowfield is caused by propagation and inversion of the pressure gradient between the upstream and downstream in the interstage clearance. Moreover, the Strouhal number (St) of the oscillation flowfield is determined and analyzed, namely, the dominant nondimensional frequency is $0.20 < St < 0.26$, and the oscillation frequency is determined by the propagation's speed and distance of the pressure gradient. Particularly, the flow tends to steady at AoI ≤ 3 deg; else self-sustaining periodic oscillation flow at AoI > 3 deg tends to be stronger with increasing AoI. The mechanism that accounts for the division condition of the AoI whether the steady or unsteady flowfield of the double-wedge configuration is also clarified, namely, the relationship between the local shear layer height and the orbiter's nose height which is governed by the incidence angle determines whether the oscillation flowfield pattern occurs or not.

I. INTRODUCTION

The two-body model is the common configuration applied in aerospace vehicles, in which two-body problems with high-speed flows over themselves involve the shock interaction, which is inherently complex and important, for instance, launch vehicle stage separation, reentry of multiple vehicles or parachute system, a hypersonic vehicle launching payload, and meteoroid fragments interacting in a planetary atmosphere.[1–7] Two-stage-to-orbit (TSTO) vehicle is a typical two-body configuration application as a hypersonic launch vehicle, which meets complex aerodynamic interference at hypersonic flight conditions.[8–15] For example, the aerodynamic interference around the Sänger TSTO vehicle including shock wave-vortex interaction is complex at $Ma = 6.83$ and results that the accuracy prediction of the aerodynamics of the TSTO is challenging.[16] Decker[17] experimentally investigated the aerodynamic interactions of the two-body vehicles in parallel-staged double-wedge configuration at $Ma = 3$ and 6 and analyzed the effects of relative body size, relative positions, nose bluntness, and lifting surface

on the longitudinal aerodynamic characteristics. Moelyadi *et al.*[18] studied the aerodynamic interferences and characteristics of TSTO at different two-stage relative positions under different Mach numbers. The results showed that mutual interferences were caused by the incident and reflected shock waves and expansion waves. Cvrlje *et al.*[19] investigated the unsteady flow around a two-body model at $Ma = 6.8$. The results showed that unsteadiness should be carefully considered because it affects the vehicles' stability. Ozawa *et al.*[20] studied the hypersonic flows over a two-body model in the shock tunnel at $Ma = 8.1$. They analyzed the effect of the clearance on the aerodynamic interference between two-body. The results showed that the shock interaction feedback mechanism caused the unsteady flow at certain clearance conditions. Wang[3] investigated the flow mechanism of the unsteady separation of the parallel-staged two-body configuration at hypersonic speeds by computational fluid dynamics (CFD) simulations and wind tunnel tests. Specifically, Wang *et al.*[8] and Wang and Wang[14] performed the unsteady numerical simulations for hypersonic separation of the
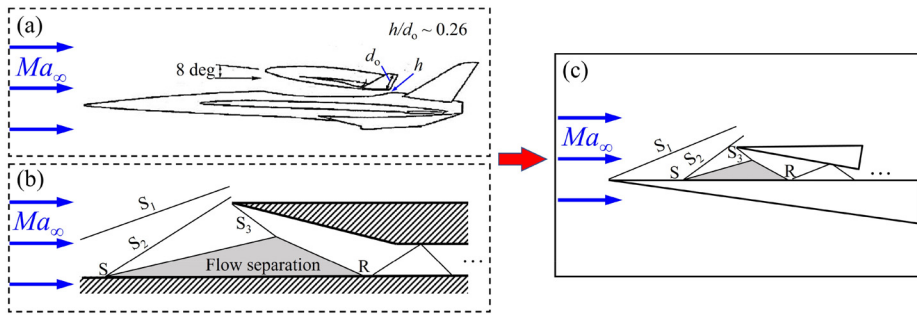
FIG. 1. The high-speed flowfield around the TSTO vehicles (a) and the large-scale separation flowfield in the two-dimensional inlet without starting (b) can be modeled into the high-speed flowfield around the double-wedge configuration (c), in which S1 is the leading-edge shock, S2 is the induced separation shock, S3 is the incident shock, S is the separation point, and R is the reattachment point.

two-body vehicle at $Ma = 6.7$. They investigated the unsteady interaction mechanism of the dynamic shock interaction and separation motion coupling. In addition, Wang et al.[21] numerically studied the separation of the parallel-staged double-wedge model at $Ma = 7$. The results showed that the complex aerodynamic interference of the two-body is composed of shock wave-shock wave interaction (SSI), shock wave-boundary layer interaction (SBLI), and flow separation.

The parallel-staged double-wedge model not only be investigated as the simple two-body model for TSTO vehicles but also the simple two-dimensional air inlet model for the inlet "unstart" phenomenon research of hypersonic ramjet engines.[22–24] Oswatitsch[25] considered the problem of having oxygen available at the maximum possible pressure for the rocket propulsion of a missile flying at high speed. He systematically studied the pressure recovery problems of the supersonic airflow passes through several oblique shock waves by theoretical considerations and presented several results of the experiments on the shock diffuser for making the pressure recovery take place in several shocks. He observed the complicated unsteady flow phenomena by using the Schlieren photographs that the interior of the missile is alternately filled with air up to a certain pressure and then part of this air is again forced out against the general direction flow under subcritical flow condition. However, a deeper analysis of the details and mechanism of the unsteady flow is lacking in the literature. A hypersonic inlet isolator is a key component that captures and compresses air to provide the desired air pressure for the combustor, but the back-pressure since combustion heat-release can cause the isolator flow to fluctuate. Wagner et al.[26] experimentally investigated the unsteady process of a Mach 5 hypersonic inlet unstart with particle image velocimetry and found that the strong shock-induced separation leads to a large reverse flow velocity and inlet unstart. Su and Zhang[27] numerically investigated the back-pressure effects on the hypersonic inlet-isolator pseudoshock motions and found that the back-pressure to the freestream pressure ratio increases to seventy causing the flowfield to turn unsteady and the pseudoshock oscillations. Moreover, they found that the greater the back pressure, the faster the unstart shock pushed upstream. Jia et al.[22] experimentally and numerically investigated the effects of several key factors on hypersonic inlet self-starting capability by a simple wedge-plate model. The results showed that the performance of the inlet start is closely relevant to the movement of the separation bubble, and the mechanism is still unknown. According to previous works, the hypersonic inlet unstart is an unsteady process of shock systems accompanied by strong SBLI.

In the mentioned literature, the investigated physical model in the research on the hypersonic flow over two-stage vehicles and the inlet-isolator is usually abstracted into the unsteady aerodynamic interaction

problem accompanied by an incident shock wave originates on the upper body (wedge or plate) impinges on the boundary layer attached on the opposite body (wedge or plate). As a result, the SBLI with shock-induced flow separation and reflected shock train occur between two-body configurations. Furthermore, the shock wave structures and flow separation of hypersonic flowfields around the TSTO vehicle with the angle of incidence (AoI) and the two-dimensional inlet of the airbreathing ramjet engine are the nearly same. Therefore, in this study view, the high-speed flows over TSTO vehicles or the ramjet engine inlet unstart problems can be characterized and simplified to the double-wedge (or wedge-plate) model[28] in high-speed flows as shown in Fig. 1. Although somewhat idealized, the problem as studied captures much of the key physics of the situations described above, and it is expected to give insight into more realistic scenarios and obtain a universal flow mechanism for a two-body model traveling in hypersonic speeds and the hypersonic inlet-isolator unstart. Moreover, some well-job studies almost focused on the hypersonic flows over the tandem-staged double-wedge model.[29–31] Still, the high-speed flow mechanism of the parallel-staged double-wedge lacks deep understanding. Moreover, the effects of the clearance or the back pressure on the unsteady hypersonic flows over the parallel-staged two-body (or two-dimensional inlet) configuration have been studied. However, the effects of the AoI on the two-body configuration are not clear yet, especially on the unsteady flowfield characteristics. In addition, the approximately $Ma = 7$ flight speed is a typical work Mach number for the ramjet engine and also the stage separation Mach number for the parallel-staged TSTO vehicles. Therefore, the paper numerically investigates the hypersonic flows over a parallel-staged double-wedge model of different AoIs at $Ma = 7$ to excavate the key flow phenomena and mechanisms. Moreover, the effects of the AoI are examined.

II. PHYSICAL MODEL

The parallel-staged double-wedge configuration is simplified from the Sänger TSTO concept[7] by reducing the scale, and a small clearance ($h/d_o = 0.26$) exists between two wedges, as shown in Fig. 2.
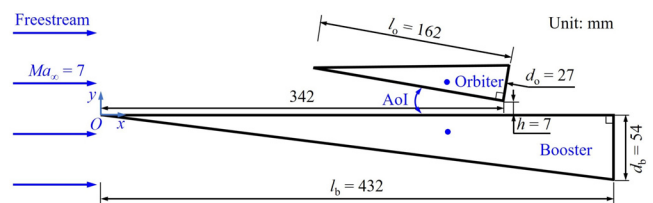

FIG. 2. The schematic illustration of the size of the double-wedge configuration.

Moreover, the decision on the scale of the clearance in the current study refers to the approximate ratio of the initial minimal clearance to the height of the orbiter of the Sänger TSTO space vehicle system as shown in Fig. 1(a). In addition, the size of this small clearance value results in the orbiter grid not intersecting with the booster's wall boundary which is convenient for the overset process of two sub-grids. In addition, the upper and lower wedges are named the orbiter and the booster, respectively. The booster and the orbiter lengths are $l_b = 432$ mm and $l_o = 162$ mm, respectively. The AoI is the angle between the orbiter's lower wall and the booster's upper wall. Furthermore, the orbiter adjusts the AoI by rotating around the fixed point, i.e., (342, 7) mm. The range of the AoI investigated in the study refers to the release angle of the orbiter relatives to the booster for the Sänger TSTO stage separation, i.e., AoI = 8 deg, as shown in Fig. 1(a). Moreover, the effects of the variation of the AoI on the unsteady flowfield of the parallel-staged double-wedge configuration are also studied. Therefore, a series of numerical simulations of different cases of AoI = 0, 2, 3, 4, 6, 8, 10, and 12 deg are performed. In addition, the freestream's angle of attack is zero.

III. NUMERICAL PROGRAM

A. Numerical methods

The unsteady N-S equations employed for the simulations of double-wedge hypersonic flowfields are given by

$$\frac{\partial}{\partial t}\iiint_\Omega \boldsymbol{W} d\Omega + \oiint_{\partial\Omega} (\boldsymbol{F}_c - \boldsymbol{F}_v) d\boldsymbol{S} = 0, \tag{1}$$

where $\boldsymbol{W}$, $\boldsymbol{F}_c$, and $\boldsymbol{F}_v$ are the vectors of conservative variables, convective fluxes, and viscous fluxes, respectively, which are expressed as

$$\boldsymbol{W} = \begin{pmatrix} \rho \\ \rho u \\ \rho v \\ \rho E \end{pmatrix}, \boldsymbol{F}_c = \begin{pmatrix} \rho \boldsymbol{V}_n \\ \rho u \boldsymbol{V}_n + n_x p \\ \rho v \boldsymbol{V}_n + n_y p \\ \rho H \boldsymbol{V}_n \end{pmatrix}, \boldsymbol{F}_v = \begin{pmatrix} 0 \\ n_x \tau_{xx} + n_y \tau_{xy} \\ n_x \tau_{yx} + n_y \tau_{yy} \\ n_x \Theta_x + n_y \Theta_y \end{pmatrix}, \tag{2}$$

where ρ is the density, u and v are the velocity components in the x and y directions, p is the pressure, and E and H are the total energy and total enthalpy per unit mass, respectively. Moreover, $p = (\gamma - 1)$ $[\rho E - 1/2\rho(u^2 + v^2)]$ and $H = E + p/\rho$, where γ is the specific heat ratio; τ_{ij} is the component of viscous stress; Θ_x and Θ_y are the heat conduction; n_x and n_y are the components of unit outward-facing

normal vector, and $\boldsymbol{V}_n$ represents the normal velocity of the control body surface. The ideal gas equation of state is introduced to close the system of equations: $p = \rho RT$.

The N-S equations are solved by the finite volume method.[32] A second-order total variation diminishing (TVD) polynomial interpolation scheme with a minmod limiter is used for spatial discretization.[33] The Harten-Lax-van Leer contact (HLLC) approximation Riemann scheme is used to compute convective flux, and the viscous flux terms are evaluated by the second-order simple average of all the vertex polynomials.[34] Additionally, Sutherland's law evaluates the viscosity and thermal conductivity coefficient. Time advancement is performed by implicit backward Euler integration with multi-grid acceleration and dual time step method.[35] In the simulations, the freestream conditions determine all conservative variables at the inflow boundary and flowfield initialization. The Mach 7 freestream conditions are $Ma_\infty = 7$, $Re_\infty = 8.60 \times 10^5$ m^{-1}, $p_\infty = 392$ Pa, $U_\infty = 2130$ m·s^{-1}, and $\rho_\infty = 0.006$ kg·m^{-3}. The conservative variables at the outflow boundary are computed from the solution in the computational domain (centroidal extrapolation). The non-slip and adiabatic conditions are adopted on the wall boundary.

B. Computational grid and verification

Since the efficiency of the overset grid methodology in solving the flowfields involves the multibody,[36] it is used for computing the flowfields for the double-wedge model. Figure 3 presents the computational overset grid and the sketch of the boundary conditions used in the simulations. The overset grid comprises two sub-grids, i.e., the booster grid is taken as a background grid and the orbiter grid is taken as a component grid. Moreover, the cutter and inner boundaries envelop the overset grid area where the flow data of two sub-grids exchange. The first cell spacing normal to the wall is chosen to ensure $y^+ \sim 1$, a progression ratio of 1.1 is applied to cluster grid points radially outward from the wall, and 40 cells spanned the thickness of the boundary layer to capture the appropriate boundary layer flow. The present study uses three grids generated by the same meshing method but with varying resolutions to verify the grid's independence. The three grids are coarse, medium, and fine grids, with approximately 80 000, 160 000, and 320 000 cells, respectively. Figure 4(a) illustrates the lift coefficients of the orbiter computed from the three grids at AoI = 8 deg. The lift coefficient calculation equation is Eq. (3), where the L is the lift. All curves of the three grids show approximately the same variation tendency with almost the same oscillation amplitude
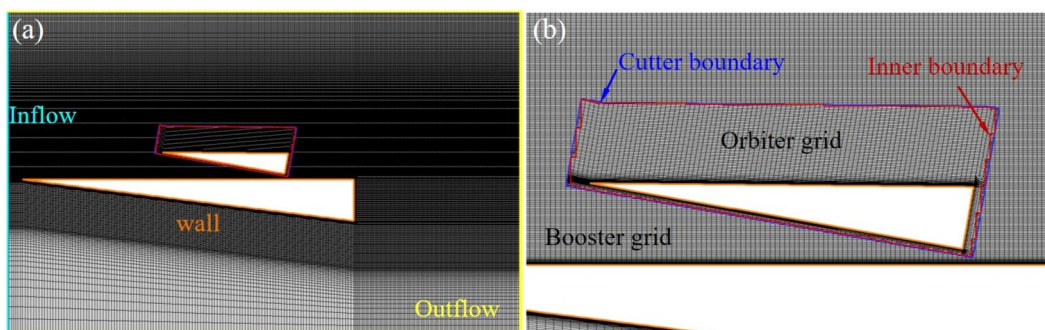

FIG. 3. The computational grid for the double-wedge configuration: (a) sketch of the boundary conditions for the grid and (b) sketch of the overset grid.
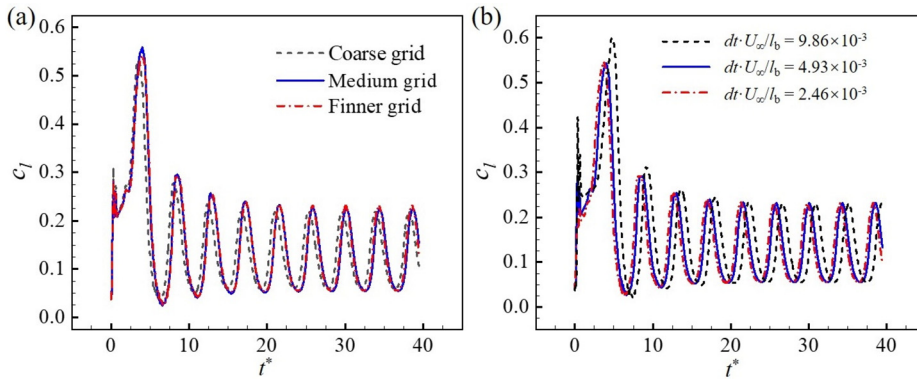
FIG. 4. Verification: (a) grid independence study and (b) time step independence study.

and periodic. Moreover, the values computed from the medium and fine grids are closer to the feature points. Therefore, the medium grid is selected for subsequent numerical simulations. In addition, the computation of the three different time steps with the same medium grid is used to verify the time step independence. The non-dimensional time steps are set as $dt \cdot U_\infty / l_b = 9.86 \times 10^{-3}$, 4.93×10^{-3}, and 2.46×10^{-3}, respectively. Figure 4(b) illustrates the lift coefficient time history of the orbiter computed with the three different time steps at AoI = 8 deg, in which the nondimensional time $t^* = t \cdot U_\infty / l_b$. All curves of these time steps show approximately the same variation tendency with almost the same oscillation amplitude and periodic. Moreover, the values computed from the $dt \cdot U_\infty / l_b = 4.93 \times 10^{-3}$ and 2.46×10^{-3} are closer to the feature points. Therefore, the time step of $dt \cdot U_\infty / l_b = 4.93 \times 10^{-3}$ is selected to obtain reliable unsteady flow-fields with computational efficiency and acceptable cost. Moreover, one period is filled with approximately 1000 computational time steps inferred from Fig. 4(b)

$$c_l = \frac{L}{\frac{1}{2}\rho_\infty U_\infty^2 l_o}. \tag{3}$$

C. Validation

In the study, the literature's shock wave-boundary layer interaction[37] is validated to determine the reliability of the same numerical methods for computing the hypersonic flowfield of the double-wedge.

The experimental data from the Mach 12.2 hypersonic laminar flows over the double-cone model in the LENS XX hypersonic wind tunnel are compared to the corresponding CFD simulation results. Figure 5 shows the computational and experimental results of the hypersonic flows over the double-cone model. The difference in the peak pressure between the CFD and the experiment is observed due to the complex separated and reattached flow region. However, the separation region and the wall pressure distribution tendency are consistent between both results. In conclusion, the comparison of the case validates the accuracy and reliability of the numerical method for double-wedge hypersonic flow.

IV. RESULTS AND DISCUSSION
A. Oscillation characteristics

Figure 6 shows the historical spatial average pressure coefficients of the interstage walls at different AoI cases. The wall pressure coefficients present periodic oscillations when AoI ≥ 4 deg but present damping oscillation and eventually tend to be steady when AoI ≤ 2 deg. Thus, the AoI that divides the two different patterns is between 2 and 4 deg. Furthermore, the oscillation wall pressure would show the oscillation flowfield with the aerodynamic interaction. In addition, the wall pressure oscillation amplitude increases with increasing AoI when AoI ≥ 4 deg while the oscillation tends to be weak and vanishes quickly then changes into steady when AoI ≤ 2 deg. Moreover, the wall pressure coefficient on the orbiter's lower wall is greater than that on the booster's upper wall, which means the
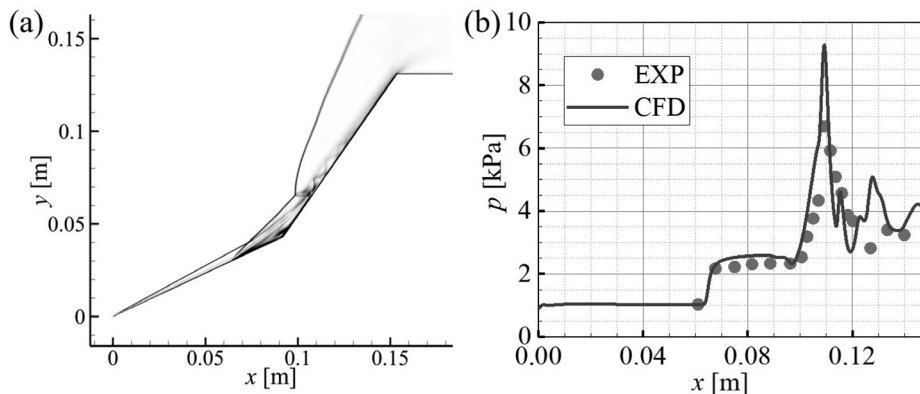

FIG. 5. The computational flowfield of hypersonic flows over the double-cone (a) and comparison of the computational and experimental wall pressure distribution (b).
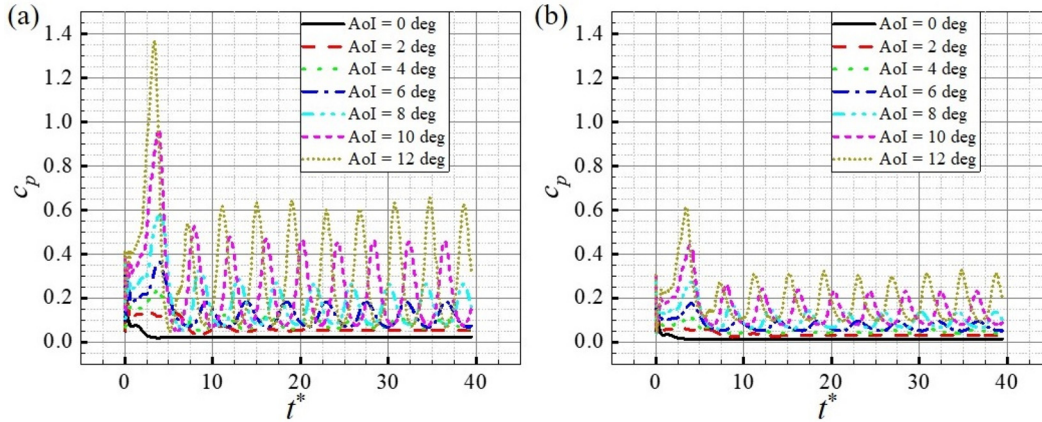
03 February 2025 14:21:18

FIG. 6. The double-wedge walls' historical spatial average pressure coefficients in different cases: (a) the orbiter's lower wall and (b) the booster's upper wall.

aerodynamic interference load on the orbiter is greater than that on the booster. Furthermore, Fig. 7 shows the fast Fourier transform (FFT) results of the spatial average pressure coefficients for the orbiter's lower wall and booster's upper wall to analyze the oscillation frequency characters, in which $St = f \cdot l_b / U_\infty$, St is the Strouhal number to describe the relationship between the frequency of periodic phenomena in fluid flow and the size of flow characteristics, and f is the frequency. Moreover, the St in terms of the dominant frequency (St_1) for $4 \deg \leq \text{AoI} \leq 12 \deg$ cases are shown respectively in Fig. 7. The St_1 increases with the AoI so that the oscillation of the double wedge flowfield tends to be strong and strong. In addition to the dominant frequency, Fig. 7 also presents the multiplication frequency with a small amplitude. Moreover, the St_1 of wall spatial average pressure coefficients are low frequencies with around $0.20 \leq St_1 \leq 0.25$ which might correspond to the large-scale flow separation with the movement of the shock structures in the inviscid flow region. In addition, the doubling frequency is around $0.4 < St_2 < 0.5$ with the small amplitude shown in Fig. 7 might correspond to the small-scale vortical flow in the recirculation region. Moreover, both FFT results of the orbiter's

lower wall and the booster's upper wall spatial average pressure coefficients show the nearly same multiplication frequency for each case respectively. Since the oscillation and frequency characters of the pressure coefficients for $4 \deg \leq \text{AoI} \leq 12 \deg$ cases are nearly the same, the AoI = 8 deg case is selected as the representation for analysis.

B. Unsteady flow characteristics

Figure 8 presents the instantaneous flowfield around the double-wedge of AoI = 8 deg and the historical Mach number distribution on the two extracted lines labeled in Fig. 8(a) to show the temporal characteristics of the unsteady flowfield. As shown in Fig. 8(a), the flowfield of the double-wedge can be characterized by leading edge shock S1, shear layer S2, and the recirculation region. Due to the flow separation induced by the incident shock wave of the obiter and the adverse pressure gradient, the recirculation region, separated shock waves S2 and S1 are moving in the oscillation way. Figures 8(b) and 8(c) present the variation of the Mach number distribution along line-1 and line-2 against time, in which the isopleths of the $Ma = 1$ and 7 are plotted by
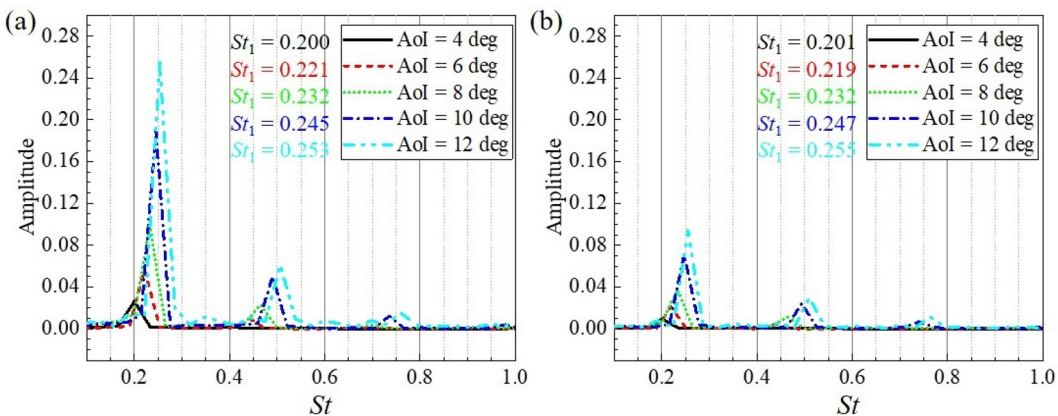
FIG. 7. The FFT results of the double-wedge walls' spatial average pressure coefficients for cases $4 \deg \leq \text{AoI} \leq 12 \deg$: (a) the orbiter's lower wall and (b) the booster's upper wall.
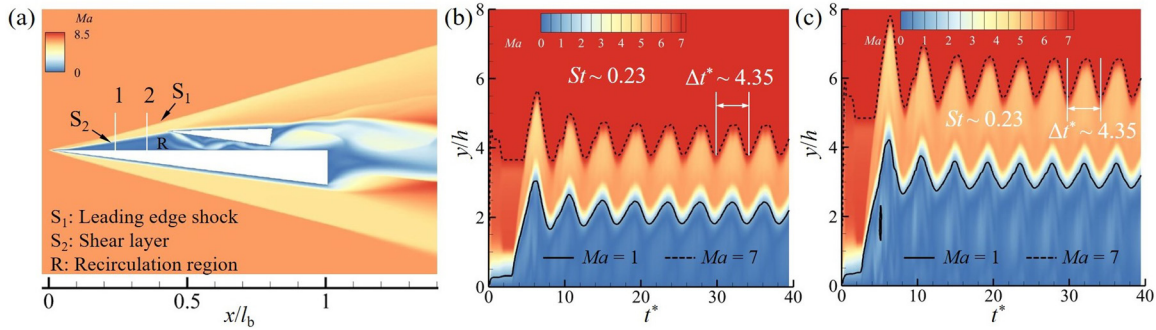
FIG. 8. The large-scale flow oscillation between the double-wedge model of AoI $= 8$ deg: (a) Mach contour of the flowfield at $t^* = 21.69$ and two extracted lines, i.e., line-1 ($x/l_b = 0.25$) and line-2 ($x/l_b = 0.35$), (b) historical Mach number on line-1, and (c) historical Mach number on line-2.

the solid and dashed lines respectively. The $Ma = 1$ isopleth indicates the periodic subsonic flow boundary traces, which equals the recirculation region boundary and shear layer. The $Ma = 7$ isopleth indicates the periodic leading edge shock traces. Moreover, the Mach contours of the two extracted lines both show the periodic oscillation behavior, indicating the unsteady periodic flowfield including the oscillations of the leading edge shock and separated shear layer. Furthermore, the leading edge shock and shear layer oscillations are synchronous since the moving of the leading edge shock (variation of the shock angle) depends on the separated shear layer. Meanwhile, the large recirculation region occurs on the booster's upper wall. They both represent the large-scale flow structure with low frequency. Moreover, the period and the St of the historical Mach numbers on line-1 and line-2 are nearly the same whose St being around 0.23, which approaches the dominant frequency of $St \sim 0.23$ as shown in Fig. 7. Therefore, the oscillation movement of the large-scale flow structures, i.e., leading edge shock, shear layer, and separation bubble, is responsible for the dominant low frequency with large amplitude in the unsteady flowfield of the double wedge.

Figure 9 shows the frequency character of the different probed points distributed along the booster's upper wall and the recirculation region for the AoI $= 8$ deg case. As shown in Fig. 9, some probed points in the flowfield show the multiplication frequency character due to the recirculation region's unsteady and complex vortical flow.

However, the probed points that are not located at the vortex center mainly show the dominant frequency ($St_1 = 0.242$) with small amplitude, such as points ($x/l_b = 0.25$, 0.35, $y/h = 0$, 0.5). Flow variables on these points may only influenced by the periodic variation of the large flow structures such as the separated shear layer. Moreover, the remaining probed points show a notable multiplication frequency (St_1–St_7) with a larger amplitude as shown in Fig. 9. First, they show a remarkable dominant frequency due to the motion of the large flow structure. Second, they show the high-frequency character due to the periodic motion of the recirculation region, the pulsating small-scale vortex motion, and the vortex interaction in the recirculation region. Figure 10 presents the Mach number contour with the streamlines between the double-wedge of two instants in the AoI $= 8$ deg case, the streamlines visualize the vortex distribution and motion in the recirculation region. Vortex is the tendon of fluid motion, the variation of the large-scale shock and shear layer motion dominates the low frequency of the periodic oscillation flowfield, and the small-scale vortex motion and their interaction contribute to the high frequency of the unsteady flow, which both determine the frequency characteristic of the unsteady flow past the double wedge.

C. Flow mechanism

After analyzing the periodic and frequency character of the unsteady flowfield, the mechanism of the oscillation flow is analyzed
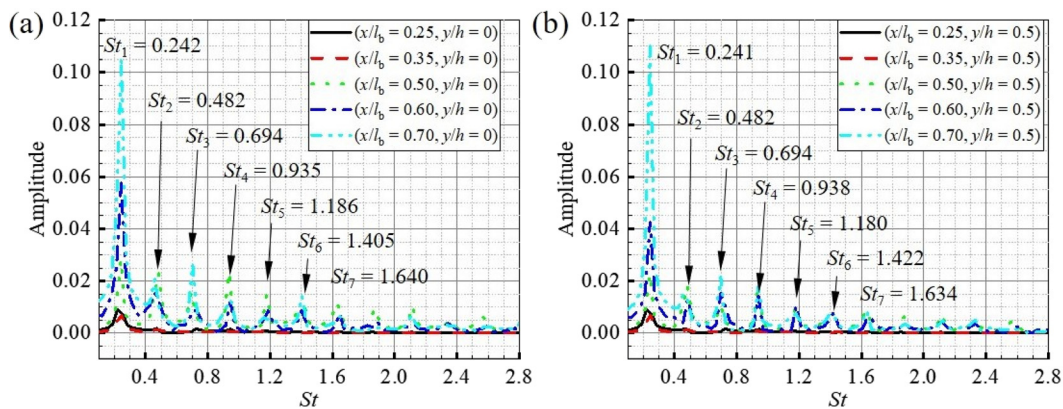

FIG. 9. The FFT results of the historical pressure for different probed points in the flowfield of AoI $= 8$ deg.
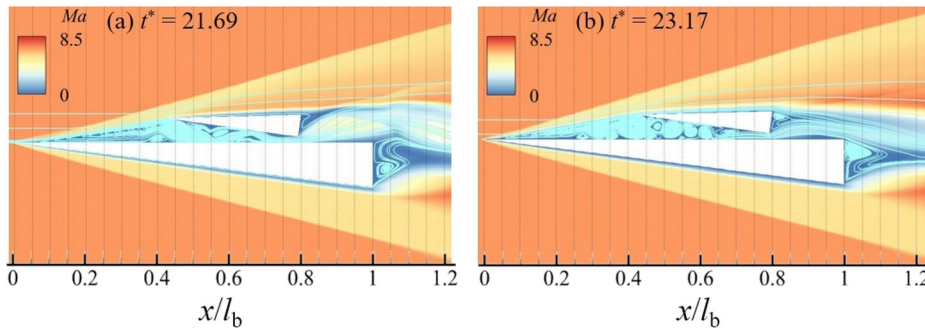
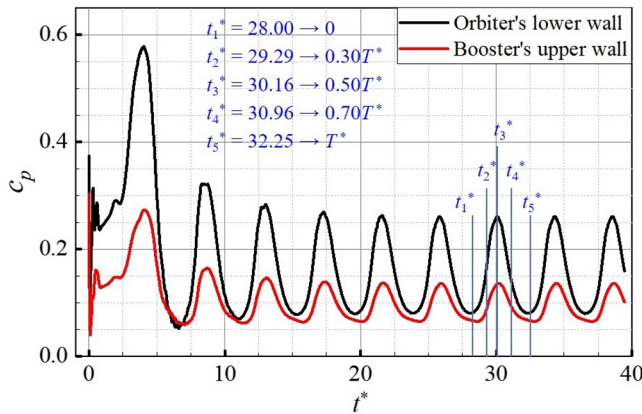**FIG. 10.** Two instantaneous flowfields of the AoI = 8 deg case.

FIG. 11. The double-wedge walls' historical spatial average pressure coefficients in the AoI = 8 deg case and five representative instants in one cycle are labeled.

as follows. To understand the periodic flow mechanism, five representative instants in an oscillation period of the spatial wall average pressure in the AoI = 8 deg case and corresponding instantaneous flowfields are presented in Figs. 11 and 12 respectively. Moreover, the variation of the pressure coefficients along the booster's upper wall and the orbiter's lower wall for different representative instants are plotted in Fig. 13. The maximum adverse pressure gradients $k = \partial c_p/\partial(x/l_b)$, i.e., the slope line of the pressure coefficient distribution, for different instants are also presented in Fig. 13. The adverse pressure gradient propagates upstream farthest and reaches the maximum when $t^* = 28.00$ or 32.34 in the periodic flow. The starting point of the one cycle for the periodic unsteady flow for analysis is defined as the adverse pressure gradient propagating near the booster's leading edge when $t^* = 28.00$ as shown in Fig. 12. The nondimensional periodic and frequency (St) for the AoI = 8 deg case are $T^* = 4.25$ and $St = 0.235$, respectively.

First, at $t_1^* = 28.00$ as shown in Fig. 12(a), a large recirculation region exists on the booster's upper wall, and the separated boundary layer transits to the shear layer. The adverse pressure gradient propagates upstream and reaches near the booster's leading edge. Therefore, the recirculation region on the booster becomes the largest during the period resulting in the booster's leading edge shock angle becoming the largest. Then the shear layer lifts and does not impinge on the orbiter so that the pressure distribution on the lower wall decreases to the valley value as shown in Figs. 12 and 13(b). In addition, the

interstage of the double-wedge is surrounded by the whole subsonic flow and the booster's lifted shear layer directly connects to the orbiter's shear layer. Moreover, the recirculation region is filled with the vortex. Due to the booster's leading edge tending to be the strongest, the pressure distribution ($0.05 < x/l_b < 0.3$) downstream of the shock and the shear layer increases to the maximum. In addition, the subsonic flow in the recirculation region passes through the interstage convergent clearance, so the pressure would decrease with the flow speed increasing [as shown in Fig. 13(a)] and achieve the sonic flow state at the clearance exit then expand to be the supersonic flow downstream. Therefore, the adverse pressure gradient tends to be the favorable pressure gradient, namely, the differential pressure between the downstream shock ($0.05 < x/l_b < 0.3$) and the interstage clearance ($0.4 < x/l_b < 0.8$) drives the subsonic flow under the shear layer downstream to the interstage clearance.

At $t_2^* = 29.29$ as shown in Fig. 12(b), the subsonic flow underneath the separated shear layer is driven by the high pressure behind the booster's leading edge shock to the downstream interstage clearance, the recirculation region moves downstream and tends to be smaller. Therefore, the angle of the booster's leading edge shock and the shear layer decreases. Moreover, the airflow speed along the shear layer increases results the strength of the shear layer increases. Furthermore, the shear layer impinges on the orbiter's nose with high flow speed so that the pressure on the orbiter increases. Specifically, the supersonic flow along the shear layer underneath the orbiter's nose induces an oblique shock wave so that a shock train[38] is formed due to the oblique shock wave reflections between stages. Furthermore, the shock train interacts with the interstage wall boundary layer, increasing the wall pressure as shown in Fig. 13. Due to the oblique shock train in the clearance, the interstage clearance airflow is divided into two recirculation regions attached to the booster and the orbiter respectively. On the other hand, another upper part of supersonic flow turns around the orbiter's nose and expands over the orbiter. Since the flow at the interstage clearance exit still keeps sonic speed and expands downstream on the booster's upper surface with the small mass flow, the wake downstream of the double wedge does not separate, consisting of the attachment vortex and several compression shock waves in the wake.

At $t_3^* = 30.16$ as shown in Fig. 12(c), the angle of the shear layer decreases further so that the induced separation shock is formed on the shear layer and converges into the booster's leading edge shock. Moreover, the airflow speed along the shear layer increases. As a result, the supersonic flow speed under the orbiter increases so that the strength of the oblique shock train in the interstage clearance increases.

(a) $t_1^* = 28.00 \rightarrow 0$

S_1: Leading edge shock
S_2: Shear layer　　　　　E: Expansion waves
S_3: Compression shock　R: Recirculation region

(b) $t_2^* = 29.29 \rightarrow 0.30T^*$

S_1: Leading edge shock　ST: Shock train
S_2: Shear layer　　　　　E: Expansion waves
S_3: Compression shock　R: Recirculation region

(c) $t_3^* = 30.16 \rightarrow 0.50T^*$

S_1: Leading edge shock
S_2: Shear layer　　　　　ST: Shock train
S_3: Separation shock　　E: Expansion waves
S_4: Compression shock　R: Recirculation region

(d) $t_4^* = 30.96 \rightarrow 0.70T^*$

S_1: Leading edge shock　S_4: Compression shock
S_2: Shear layer　　　　　E: Expansion waves
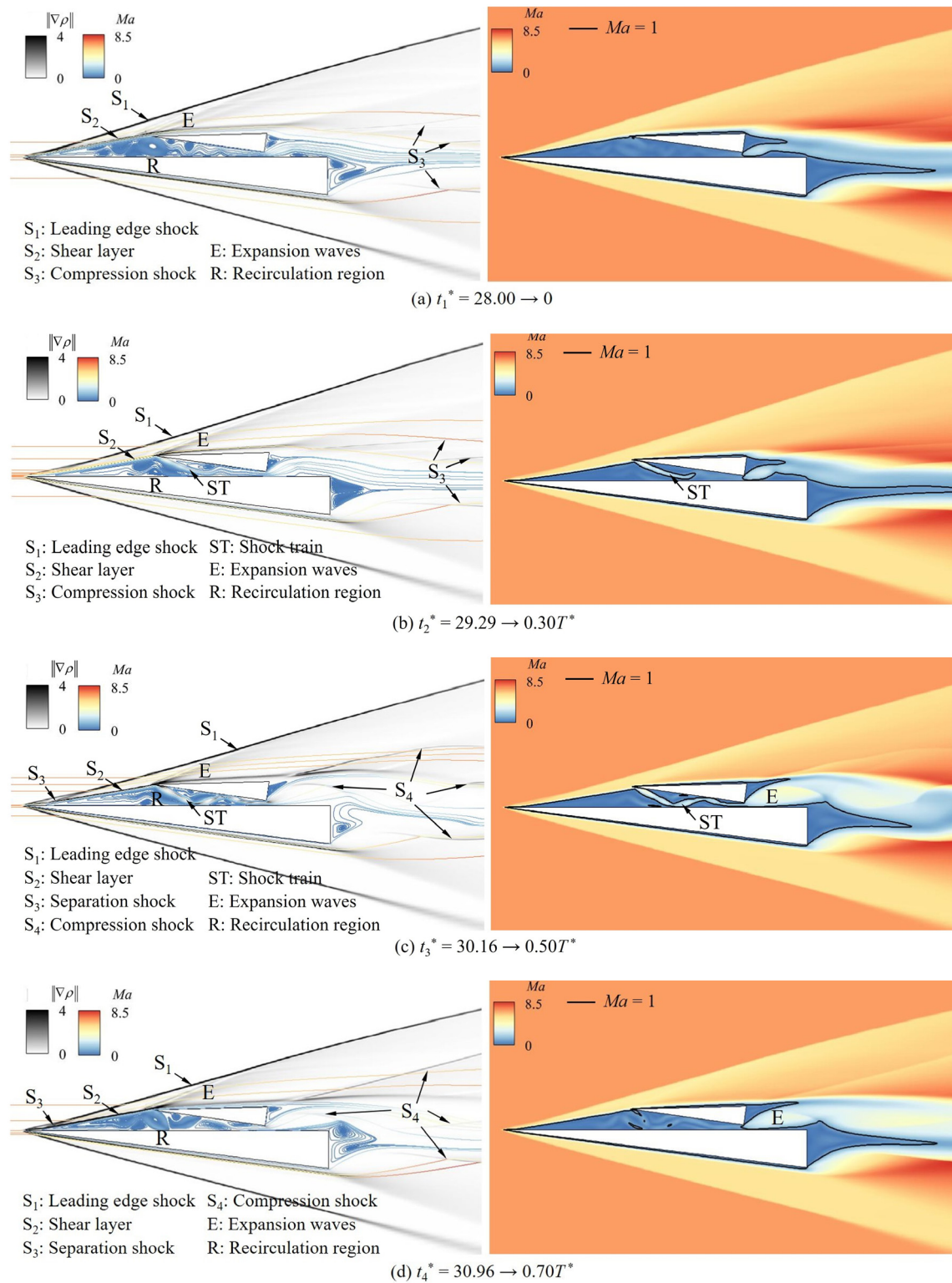S_3: Separation shock　　R: Recirculation region

FIG. 12. Representative instantaneous flowfields in one period of the periodic flow of the AoI = 8 deg case: (a) numerical schlieren and the streamlines colored by the Mach number of the flowfield and (b) Mach contours with the sonic lines of the flowfield.
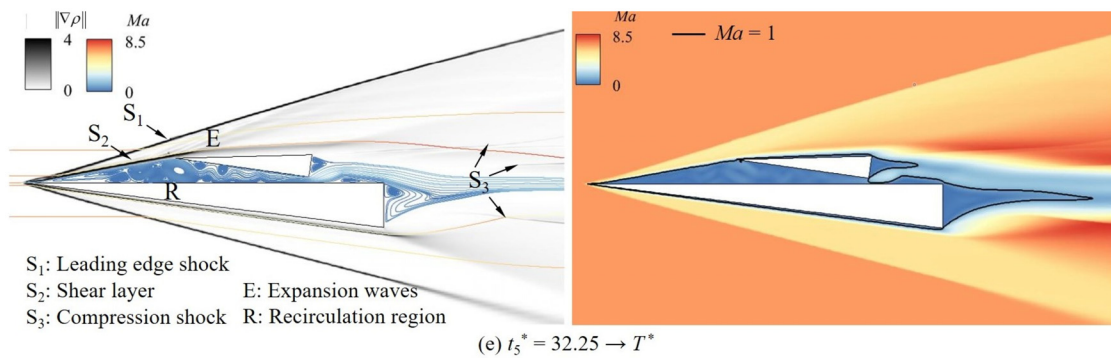
(e) $t_5^* = 32.25 \rightarrow T^*$
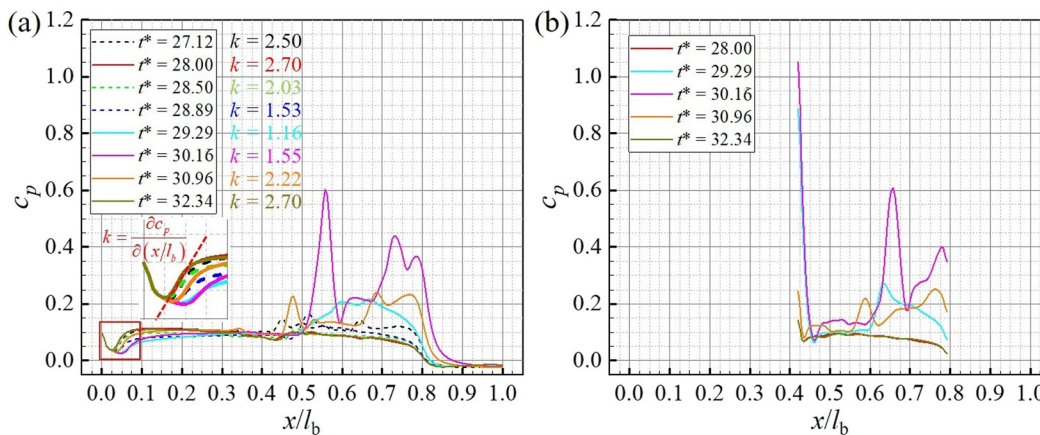
FIG. 12. (*Continued.*)

FIG. 13. The pressure coefficients along the booster's upper wall (a) and the orbiter's lower wall (b) at the representative instants during the period flow of the AoI = 8 deg case.

Moreover, the oblique shock train extends downstream and reaches the clearance exit, the interstage flow directly expands at supersonic speed in the double-wedge wake. Due to the interaction between the strong shock train and the interstage wall, the pressure in the clearance reaches the maximum, as shown in Fig. 13. The separation bubbles are split by the oblique shock train to attach to the wall so that the motion of vortexes becomes regular and predictable. At the same time, due to the reflections of the oblique shock train on the wall, the flow pressure at the clearance exit increases. Hence, the wake of the double-wedge begins to separate and behaves in an oscillation way with the deformation of compression shock waves, and the attachment vortexes on the stages' back move upward. The maximum adverse pressure gradient is formed at this instant and ready to propagate upstream through the subsonic recirculation region.

At $t_4^* = 30.96$ as shown in Fig. 12(d), the adverse pressure gradient in the interstage clearance propagates upstream through the recirculation region resulting in the separation bubbles attached to the interstage walls moving upstream and the vanish of the shock train. Furthermore, the shear layer is lifted by the moving upstream vortex in the expanding recirculation region. As the shear layer is lifted, the

induced separation shock moves upstream and converges into the booster's leading edge shock. The impingement position of the shear layer on the obiter moves upward and turns around the orbiter's nose. Then the raised shear layer develops downstream over the orbiter and causes the compression shock to be formed in the wake. Due to the impingement point of the shear layer on the obiter moving upward, the strength of the shock train in the clearance decreases. Thus, the oblique shock train vanishes quickly, and the interstage wall pressure decreases (as shown in Fig. 13) due to the absence of the interaction between the shock train and the interstage wall. With the flow pressure at the clearance exit decrease, the oscillation of the wake tends to be smooth. Moreover, the compression shock wave interacts with the attachment vortex resulting in the vortex being lifted further. The downstream wake of the double-wedge is ready to converge.

At $t_5^* = 32.25$ as shown in Fig. 12(e), the separation bubbles underneath the shear layer dilate and move upstream under the driving of the adverse pressure gradient along the booster's upper wall, and the recirculation region becomes largest. Moreover, the strength of the leading edge shock reaches the maximum while the flow speed and the
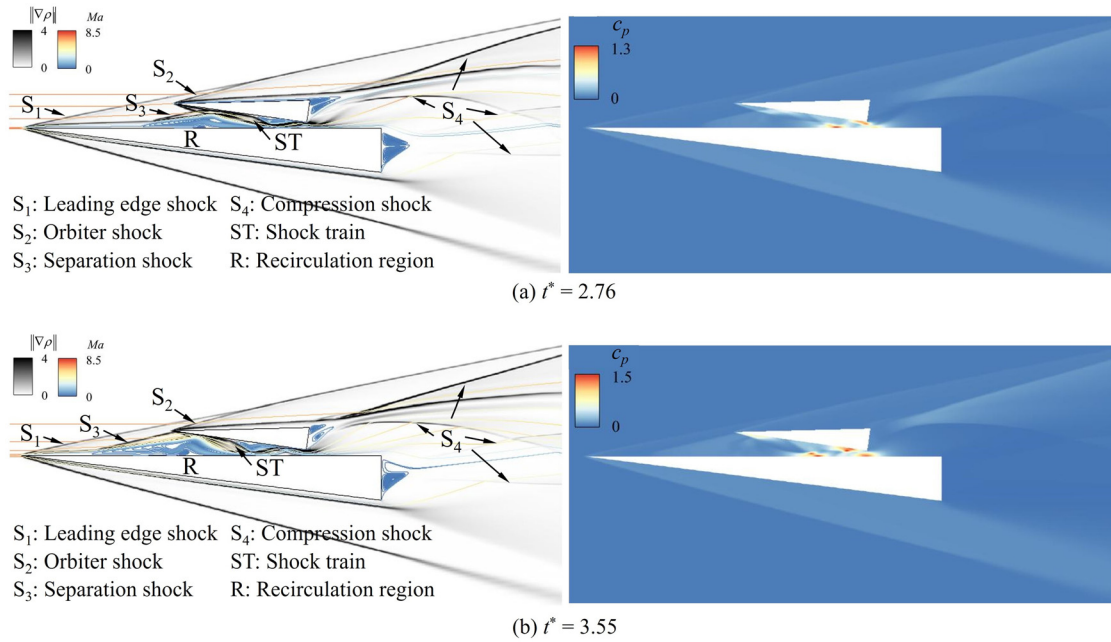
S₁: Leading edge shock   S₄: Compression shock
S₂: Orbiter shock   ST: Shock train
S₃: Separation shock   R: Recirculation region

(a) $t^* = 2.76$

S₁: Leading edge shock   S₄: Compression shock
S₂: Orbiter shock   ST: Shock train
S₃: Separation shock   R: Recirculation region

(b) $t^* = 3.55$

FIG. 14. Two instantaneous flowfields in the starting process of the AoI $= 8$ deg case: (a) numerical schlieren and the streamlines colored by the Mach number of the flowfield and (b) pressure coefficient contours of the flowfield.

pressure in the clearance decrease to the minimum. The wake downstream double-wedge mixes to be a broad one. Everything returns to the initial phase of the period (the flowfields shown in Figs. 12(a) and 12(e) are nearly the same so that a period is formed), the pressure gradient along the booster's upper wall reverses to the favored type and propagates downstream in the recirculation region, and the shock train will be formed in the clearance as the impingement of the shear layer on the orbiter's lower wall. The next period with the same aerodynamic interaction occurs between the double-wedge dawns, goes, and returns in the oscillation period without end.

The mechanism of the large recirculation region and adverse pressure gradient occurring on the booster's upper wall is declared by the flowfield starting process shown in Fig. 14. The flowfield in the clearance shows the complex aerodynamic interaction between the shock wave and the boundary layer. Therefore, the pressure in the clearance rises dramatically which results in the adverse pressure gradient on the booster's upper wall. With the pressure gradient increasing, the separated boundary layer develops upstream. It tends to be strong, and the oblique shock train caused by the reflections of the obiter shock is formed in the clearance. The induced separation shock impinges on the orbiter's nose so that the wall pressure reaches a maximum as shown in Fig. 11. The following variation of the flowfield is similar to the flowfields shown in Fig. 12, and the period flowfield of the double-wedge is formed.

In the above analysis, the mechanism that accounts for the oscillation flowfield of the double wedge is the pressure gradient propagating upstream and downstream through the subsonic recirculation region on the booster's upper wall. The adverse pressure gradient is formed in the interstage clearance due to the shock wave-boundary layer interaction. Then the adverse pressure gradient reverses into the

favor pressure gradient when the recirculation region extends upstream near the booster's leading edge and the strength of the booster's leading edge shock reaches maximum. Therefore, the oscillation flowfield driven by the pressure gradient in the recirculation region is formed. The propagating speed of the pressure gradient in the recirculation region plays a role in the period characteristics of the oscillation flow. The pressure gradient acts as a small disturbance whose propagating speed (u_p) equals the local sound speed (a) in the stationary gas, i.e., $u_p = a$, while $u_p = a \pm u_g$ when the disturbance propagates in the moving gas with the flow speed (u_g) of x-component, in particular, if the propagating velocity is in the same direction as the gas velocity, $u_p = a + u_g$, else if, $u_p = a - u_g$. Figure 15 plots the sonic and gas speed along the line of $y/h = 0.5$ of five instantaneous flowfields in one period to calculate the propagating speed of the pressure gradient in the recirculation region. The calculated speeds of the sonic and the gas flow are selected as average speeds in the zone of $0.15 < x/l_b < 0.8$. The statistical average speeds of the sonic, the gas flow, and the pressure gradient's propagating are presented in Table I. Therefore, the average propagating speed of the pressure gradient is around $u_p/U_\infty = 0.404$, so Eqs. (4) and (5) calculate the oscillation period and St, in which the $L_p = 0.342$ is the propagating distance between the booster's leading edge and the exit of the clearance. Hence, $T^* = 3.92$ and $St = 0.255$. The predicted periodic value approaches the FFT results ($T^* = 4.13$ and $St = 0.242$) as discussed in Fig. 9 and above periodic analysis results of the oscillation flowfield.

$$T^* = 2L_p U_\infty / u_p l_b, \tag{4}$$
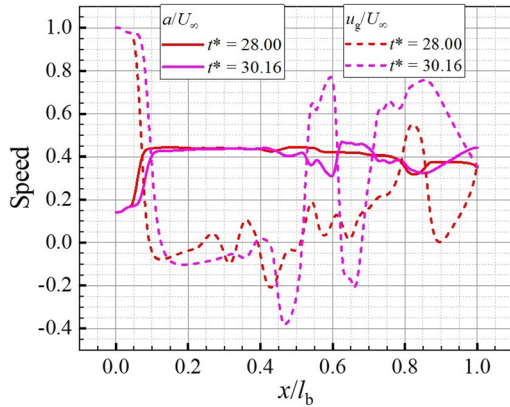
and

$$St = 1/T^*. \tag{5}$$

FIG. 15. The sonic and airflow speed distributions along the line of $y/h = 0.5$ in one oscillation flowfield of the AoI = 8 deg case.

TABLE I. The statistical average speeds of the sonic, the gas flow, and the pressure gradient's propagating.

	a/U_∞	u_g/U_∞	u_p/U_∞	Remark
$t^* = 28.00$	0.429	0.038	0.391	$u_p = a + u_g$
$t^* = 30.16$	0.418	0.105	0.313	$u_p = a - u_g$
Average	$\cdots$	$\cdots$	0.404	

D. Critical condition

The oscillation flowfield and its flow mechanism and periodic characteristics have been analyzed, and the remaining question for the unsteady flowfield past the parallel-staged double-wedge is why the AoI boundary that divides the steady and oscillation flowfield patterns is between 2 and 4 deg. Figure 16 shows the steady flowfield and unsteady flowfields past the double-wedge configuration for AoI = 2 and 4 deg, respectively. The major difference in flowfield for the two cases is that the separated shear layer rises over the orbiter just right and then connects with the orbiter's boundary layer since the small incidence angle of the orbiter as shown in Fig. 16(a) instead of impinging directly on the orbiter's nose so that induce the oblique shock train and adverse pressure rising in the interstage clearance as shown in Figs. 16(b)–16(d). Figure 17 plots the pressure coefficients along the booster's upper wall in the flowfields presented in Fig. 16 for AoI = 2 and 4 deg cases. Since the absence of the impingement of the separated shear layer on the orbiter's nose, the little strength of the adverse pressure gradient underneath the orbiter's nose causes a steady and small separated bubble in front of the orbiter. However, as the orbiter's incidence angle rises slightly to the AoI = 4 deg, the stronger pressure is induced under the impingement of the separated shear layer and the interaction between the shock train and the interstage walls. As a result, the adverse pressure gradient overcomes the viscous of the wall boundary layer and drives the recirculation region to extend and move upstream then performs the oscillation flowfield pattern as discussed previously. Therefore, for the parallel-staged double-wedge configuration, the relationship between the local shear layer height and the orbiter's nose height which is governed by the incidence angle
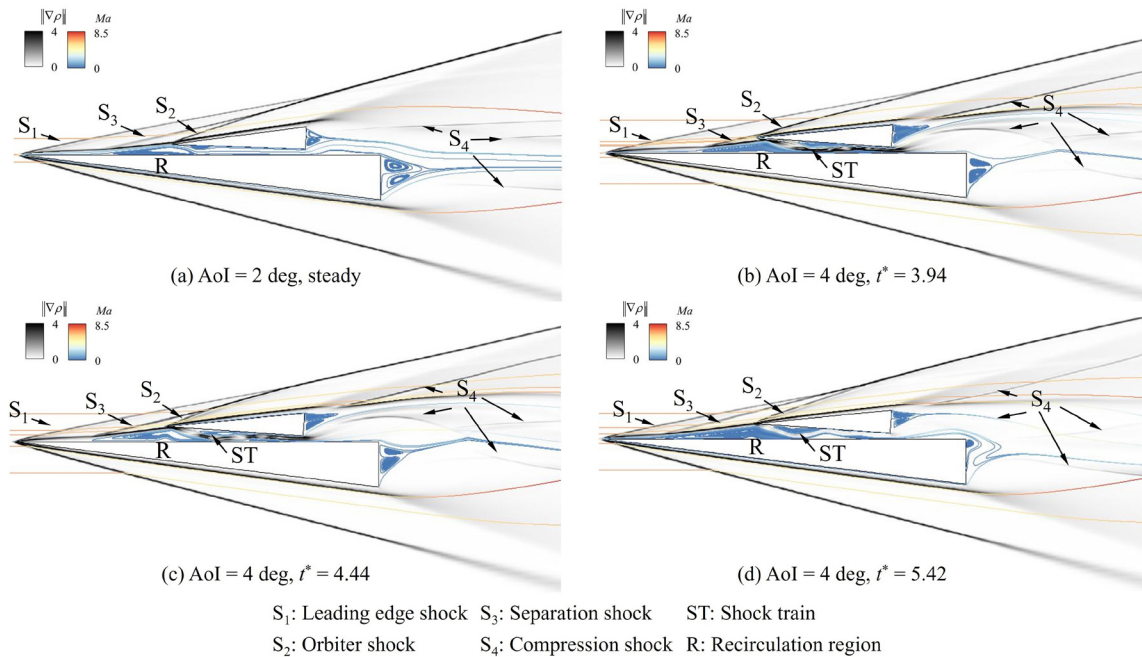

(a) AoI = 2 deg, steady

(b) AoI = 4 deg, $t^* = 3.94$

(c) AoI = 4 deg, $t^* = 4.44$

(d) AoI = 4 deg, $t^* = 5.42$

S_1: Leading edge shock S_3: Separation shock ST: Shock train
S_2: Orbiter shock S_4: Compression shock R: Recirculation region

FIG. 16. The flowfields past the double wedge configuration for AoI = 2 deg (a) and 4 deg (b)–(d) respectively.
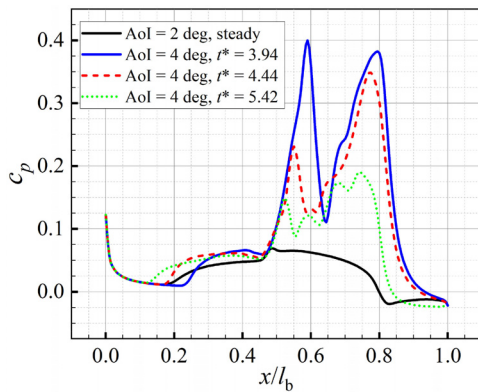
FIG. 17. The pressure coefficients along the booster's upper wall for AoI = 2 and 4 deg, respectively.

determines whether the oscillation flowfield pattern occurs or not. The oscillation strength is increasing with the AoI, but, the oscillation temporal characteristic is determined by the propagating speed of the pressure gradient in the recirculation region in the interstage clearance.

Therefore, for the parallel-staged double-wedge configuration, the relationship between the local shear layer height and the orbiter's nose height which is governed by the incidence angle determines whether the oscillation flowfield pattern occurs or not. Figure 18 plots the heights of the orbiter's nose and local shear layer in front of the orbiter at different AoI cases. As shown in Fig. 18, the height of the shear layer is larger than the height of the orbiter's nose when the AoI < 3 deg and reversely when the AoI > 3 deg. Hence, the flowfield is the damping oscillation and tends to steady when the AoI < 3 deg due to the absence of the strong shock train while the flowfield is unsteady periodic oscillation when the AoI > 3 deg due to the strong shock train between the clearance. The critical condition for the flowfield pattern whether periodic or damping oscillation is that AoI around 3 deg.

To determine and validate that the critical AoI condition is between 2 and 4 deg, the unsteady numerical simulation of the AoI = 3 deg for the parallel-staged double-wedge case is performed at
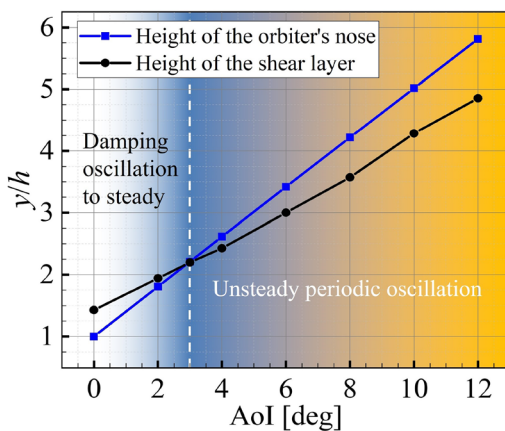

FIG. 18. The heights of the local shear layer in front of the orbiter's nose and the orbiter's nose in different AoI cases.

last. Figure 19 presents the numerical result which shows a damping oscillation flow behavior and validates the inference that the critical AoI condition is AoI = 3 deg of dividing the steady and unsteady periodic oscillation flowfield for the double-wedge configuration. As shown in Fig. 19(a), the average pressure coefficients of the interstage walls present the damping oscillation characteristics. The oscillation amplitude decreases continuously with the increase in time and finally decreases to zero so that the wall pressure tends to the steady state. Moreover, Fig. 19(b) shows the time history of the Mach number along the probed line ($x/l_b = 0.35$), and the Mach contour also shows the damping oscillation characteristic. Furthermore, the St of the damping oscillation is around 0.20. In addition, in contrast to the unsteady oscillation flowfields of the larger AoI cases, the flow structure affected by the fluctuation at the AoI = 3 deg is less, e.g., the leading edge shock is not affected as shown by the steady isoline of $Ma = 7$. Figure 19(c) shows two instantaneous flowfields when the flowfield dampens oscillation and steady-state respectively. The supersonic separated shear layer impinges on the orbiter's nose just right, and a weak shock train is induced in the clearance. Then, the weak shock train induces the wall pressure to increase slightly and causes the flow separation on the booster. Moreover, the recirculation region increases the shear layer's height and the shear layer induces the separation shock as shown in Fig. 19(c). However, with the upraise of the shear layer, the shear layer will rise over the orbiter's nose so that the strength of the shock train will decrease and the wall pressure on the booster decreases. Then, the adverse pressure gradient in the clearance tends to be smaller, and the recirculation region on the booster is small resulting in the shear layer subsiding slightly, so the shear layer impinges on the orbiter's nose associated with the weaker shock train. Therefore, the damping oscillation is formed. As time passes, the separated shear layer, recirculation region, and shock train will form a balance between each other in the clearance given the AoI = 3 deg. Finally, the flowfield tends to a steady state which the very weak shock train formed in the clearance to maintain the little adverse pressure gradient for the small recirculation region on the booster and also the separated shear layer impinging on the orbiter's nose as shown in Fig. 19(c).

V. CONCLUSIONS

This paper numerically investigates the unsteady flow past the parallel-staged double-wedge configuration at $Ma = 7$ for different AoI cases. Moreover, the time-variation pressure coefficient, unsteady characteristics including periodic and frequency, and flow mechanism with aerodynamic interaction are analyzed and revealed. The effects of the AoI on the flowfield are also analyzed. The results show that the flowfield presents the periodic oscillation characteristics when the AoI > 3 deg while the flowfield tends to be steady when the AoI ≤ 3 deg. The aerodynamic interaction of the double-wedge configuration tends to be stronger with the increase in AoI, and the oscillation frequency increases slightly with the increases in AoI. The nondimensional dominant frequency of the oscillation flowfields for $4 \leq$ AoI ≤ 12 deg cases varies between $0.20 < St < 0.26$. The double-wedge's oscillation flowfield is the pressure gradient propagating upstream and downstream through the subsonic recirculation region on the booster's upper wall. The adverse pressure gradient is formed in the interstage clearance due to the shock wave-boundary layer interaction and the reflections of the shock train. Moreover, the relationship between the local shear layer height and the orbiter's nose height which is governed by the incidence angle determines whether the oscillation
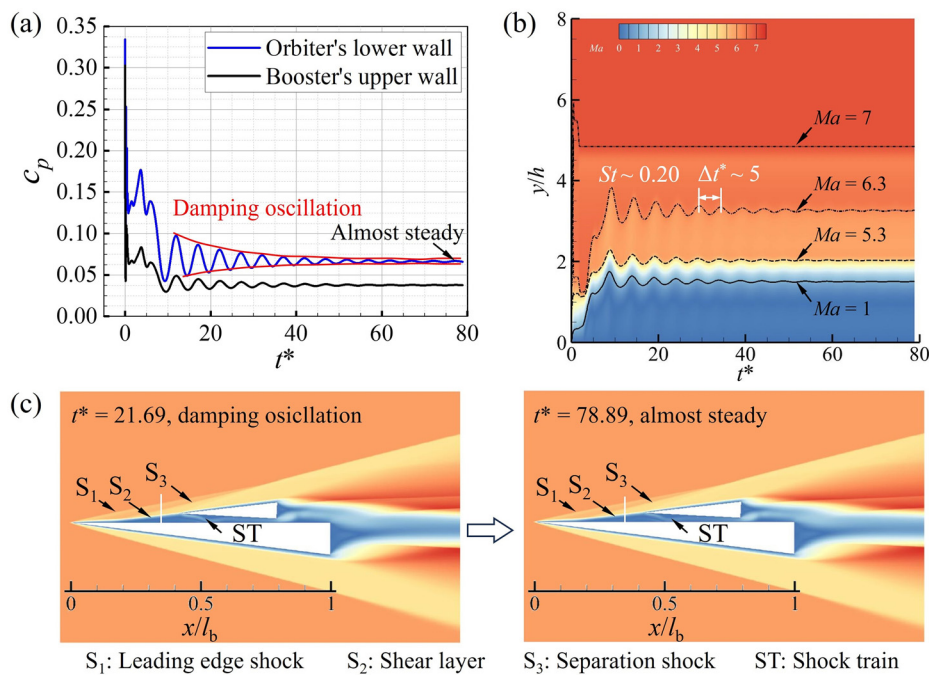
FIG. 19. Flowfield of the AoI = 3 deg case: (a) the double-wedge walls' historical spatial average pressure coefficients, (b) historical Mach number on extracted line ($x/l_b = 0.35$), and (c) two typical instantaneous flowfields.

flowfield pattern occurs or not. The oscillation temporal characteristic is determined by the propagating speed of the pressure gradient in the recirculation region in the interstage clearance.

AUTHOR DECLARATIONS
Conflict of Interest

The authors have no conflicts to disclose.

Author Contributions

Yue Wang: Conceptualization (equal); Data curation (equal); Formal analysis (equal); Investigation (equal); Methodology (equal); Visualization (equal); Writing – original draft (equal); Writing – review & editing (equal). **Yiming Liu:** Conceptualization (supporting); Methodology (supporting); Writing – review & editing (equal). **Haojie Li:** Conceptualization (supporting); Writing – review & editing (equal). **Xiaopeng Xue:** Conceptualization (equal); Data curation (equal); Methodology (equal); Resources (equal); Supervision (lead); Writing – review & editing (lead). **Yunpeng Wang:** Conceptualization (supporting); Data curation (equal); Funding acquisition (lead); Methodology (equal); Project administration (equal); Resources (equal); Supervision (equal); Writing – review & editing (equal).

DATA AVAILABILITY

The data that support the findings of this study are available from the corresponding author upon reasonable request.

REFERENCES

[1]Y. P. Wang, H. Ozawa, H. Koyama, and Y. Nakamura, "Abort separation of launch escape system using aerodynamic interference," AIAA J. **51**, 270–275 (2013).

[2]S. H. Park, S. Kim, I. Choi, and G. Park, "Experimental study of separation behavior of two bodies in hypersonic flow," Acta Astronaut. **181**, 414–426 (2021).

[3]Y. Wang, "Investigation on flow mechanism and safe separation scheme for parallel-staged two-body configuration," Ph.D. dissertation (University of Chinese Academy of Sciences, Beijing, 2024) (in Chinese).

[4]M. Patel and S. Navarro-Martinez, "Heat transfer to proximal cylinders in hypersonic flow," Phys. Fluids **35**, 036125 (2023).

[5]L. Jiang, H. Jia, X. Xu, W. Rong, Q. Wang, G. Chen, J. Fan, and X. Xue, "Effect of different geometric porosities on aerodynamic characteristics of supersonic parachutes," Space Sci. Technol. **3**, 0062 (2023).

[6]H. Jia, W. Bao, W. Rong, Y. Li, X. Xue, and J. Fan, "Numerical study on aerodynamic characteristics of parachute models for future Jupiter exploration," Space Sci. Technol. **4**, 0116 (2024).

[7]H. Kuczera and P. W. Sacher, *Reusable Space Transportation Systems* (Springer, Berlin Heidelberg, 2011).

[8]Y. Wang, Y. P. Wang, and Z. L. Jiang, "Unsteady interaction mechanism of transverse stage separation in hypersonic flow for a two-stage-to-orbit vehicle," Phys. Fluids **35**, 056120 (2023).

[9]Y. Wang, Y. P. Wang, and Z. L. Jiang, "Numerical investigation of aerodynamic separation schemes for two-stage-to-orbit-like two-body system," Aerosp. Sci. Technol. **131**(Part A), 107995 (2022).

[10]Y. Wang, Y. P. Wang, C. Wang, and Z. L. Jiang, "Numerical study of longitudinal stage separation for parallel-staged two-stage-to-orbit vehicle," Acta Aeronaut. Astronaut. Sin. **44**, 127634 (2023) (in Chinese).

[11]Y. Wang, Y. P. Wang, C. Wang, and Z. L. Jiang, "Numerical investigation on longitudinal stage separation of spiked two-stage-to-orbit vehicle," J. Spacecr. Rockets **60**, 215–229 (2023).

[12]Y. Wang, Y. P. Wang, and Z. L. Jiang, "Experimental study of longitudinal stage separation of two-body configuration in shock tunnel," AIAA J. **60**, 6940–6946 (2022).

[13]Y. Wang, Y. P. Wang, and Z. L. Jiang, "Test technology of longitudinal stage separation for two-stage-to-orbit vehicle in shock tunnel," Acta Aeronaut. Astronaut. Sin. **44**, 128126 (2023) (in Chinese).

[14]Y. Wang and Y. P. Wang, "Unsteady interaction and dynamic stability analysis of a two-stage-to-orbit vehicle during transverse stage separation," Acta Astronaut. **216**, 488–503 (2024).

[15]Y. Wang, Y. P. Wang, and Z. L. Jiang, "Experimental and numerical investigation on the unsteady interaction in longitudinal stage separation for parallel-staged two-body configuration," Phys. Fluids **36**, 016116 (2024).

[16]W. Schroder and G. Hartmann, "Analysis of inviscid and viscous hypersonic flows past a two-stage spacecraft," J. Spacecr. Rockets **30**, 8–13 (1993).

[17]J. P. Decker, *Aerodynamic Interference Effects Caused by Parallel-Staged Simple Aerodynamic Configurations at Mach Numbers of 3 and 6* (NASA Langley Research Center Hampton, NASA-TN-D-5379, Washington, DC, 1969).

[18]M. A. Moelyadi, C. Breitsamter, and B. Laschka, "Stage-separation aerodynamics of two-stage space transport systems part1: Steady-state simulations," J. Spacecr. Rockets **45**(6), 1230–1239 (2008).

[19]T. Cvrlje, C. Breitsamter, and B. Laschka, "Numerical simulation of the lateral aerodynamics of an orbital stage at stage separation flow conditions," Aerosp. Sci. Technol. **4**, 157–171 (2000).

[20]H. Ozawa, K. Kitamura, K. Hanai, K. Mori, and Y. Nakamura, "Unsteady aerodynamic interaction between two bodies at hypersonic speed," Trans. Jpn. Soc. Aeronaut. Space Sci. **53**, 114–121 (2010).

[21]Y. Wang, Y. P. Wang, X. P. Xue, and Z. L. Jiang, "Numerical investigation on safe stage separation problem of a TSTO model at Mach 7," Chin. J. Theor. Appl. Mech. **54**, 526–542 (2022) (in Chinese).

[22]Y. N. Jia, L. J. Yue, and X. Y. Chang, "The phenomena of sudden change in hypersonic inlets self-starting capability," in 21st AIAA International Space Planes and Hypersonics Technologies Conference, AIAA Paper No. AIAA 2017-2188, 2017.

[23]S. Z. Yang, W. Z. Xie, C. L. Xu, and G. F. Ma, "Generalized prediction for self-starting performance of two-dimensional hypersonic inlets," Phys. Fluids **36**(1), 015129 (2024).

[24]X. T. Tong, L. J. Yue, W. N. Wu, Q. F. Zhang, and H. Chen, "Self-similar unstart characteristics of supersonic contraction duct with an expansion corner," Phys. Fluids **36**(1), 016148 (2024).

[25]K. Oswatitsch, "Pressure recovery for missiles with reaction propulsion at high supersonic speeds (the efficiency of shock diffusers)," in *Contributions to the Development of Gasdynamics: Selected Papers, Translated on the Occasion of K. Oswatitsch's 70th Birthday* (Vieweg+ Teubner Verlag, Wiesbaden, 1980), pp. 290–323.

[26]L. Wagner, K. B. Yuceil, A. Valdivia, N. T. Clemens, and D. S. Dolling, "PIV measurements of the unstart process in a supersonic inlet/isolators," in 38th Fluid Dynamics Conference and Exhibit, AIAA Paper No. AIAA 2008-3849, 2008.

[27]W. Y. Su and K. Y. Zhang, "Back-pressure effects on the hypersonic inlet-isolator pseudoshock motions," J. Propul. Power **29**(6), 1391–1399 (2013).

[28]J. M. Yang, Z. F. Li, Y. J. Zhu, E. L. Zhang, and J. Wang, "Shock waves and shock interactions in hypersonic flow," (National Defense Industry Press, Beijing, 2019) (in Chinese).

[29]O. Tumuklu and K. M. Hanquist, "Temporal characteristics of hypersonic flows over a double wedge with Reynolds number," Phys. Fluids **35**(10), 106116 (2023).

[30]A. A. Ray and A. De, "Leading-edge bluntness effects on the hypersonic flow over the double wedge at multiple aft-wedge angles," Phys. Fluids **35**(5), 056116 (2023).

[31]G. Kumar and A. De, "Modes of unsteadiness in shock wave and separation region interaction in hypersonic flow over a double wedge geometry," Phys. Fluids **33**, 076107 (2021).

[32]S. Chakravarthy, "A unified-grid finite volume formulation for computational fluid dynamics," Int. J. Numer. Methods Fluids **31**, 309–323 (1999).

[33]E. F. Toro, *Riemann Solvers and Numerical Methods for Fluid Dynamics: A Practical Introduction* (Springer Science & Business Media, New York, 2009).

[34]H. Luo, J. Baum, and R. Lohner, "Extension of HLLC scheme for flows at all speeds," in *16th AIAA Computational Fluid Dynamics Conference*, AIAA Paper No. AIAA 2003–3840, 2003.

[35]J. R. Edwards, "An implicit multigrid algorithm for computing hypersonic, chemically reacting viscous flows," J. Comput. Phys. **123**, 84–95 (1996).

[36]S. L. Tian, J. W. Fu, and J. T. Chen, "A numerical method for multi-body separation with collisions," Aerosp. Sci. Technol. **109**, 106426 (2021).

[37]M. S. Holden, M. MacLean, T. P. Wadhams, and A. Dufrene, "Measurements of real gas effects on regions of laminar shock wave/boundary layer interaction in hypervelocity flows for "blind" code validation studies," in 21st AIAA Computational Fluid Dynamics Conference, AIAA Paper No. AIAA 2013–2837, 2013.

[38]H. J. Tan, S. Sun, and H. X. Huang, "Behavior of shock trains in a hypersonic inlet/isolator model with complex background waves," Exp. Fluids **53**, 1647–1661 (2012).

03 February 2025 14:21:18